Physical interpretation and separation of eddy current pulsed thermography

Aijun Yin, Bin Gao, Gui Yun Tian, W. L. Woo, and Kongjing Li

Citation: J. Appl. Phys. **113**, 064101 (2013); doi: 10.1063/1.4790866
View online: http://dx.doi.org/10.1063/1.4790866
View Table of Contents: http://jap.aip.org/resource/1/JAPIAU/v113/i6
Published by the American Institute of Physics.

Physical interpretation and separation of eddy current pulsed thermography

Aijun Yin,[1,2,a)] Bin Gao,[2,3,a),b)] Gui Yun Tian,[2,3] W. L. Woo,[2] and Kongjing Li[2]
[1]*The State Key Laboratory of Mechanical Transmission, College of Mechanical Engineering, Chongqing University, Chongqing 400044, China*
[2]*School of Electric and Electronic Engineering, Newcastle University, England, United Kingdom*
[3]*School of Automation Engineering, University of Electronic Science and Technology of China, Chengdu, China*

(Received 30 December 2012; accepted 25 January 2013; published online 8 February 2013)

Eddy current pulsed thermography (ECPT) applies induction heating and a thermal camera for non-destructive testing and evaluation (NDT&E). Because of the variation in resultant surface heat distribution, the physical mechanism that corresponds to the general behavior of ECPT can be divided into an accumulation of Joule heating via eddy current and heat diffusion. However, throughout the literature, the heating mechanisms of ECPT are not given in detail in the above two thermal phenomena and they are difficult to be separated. Nevertheless, once these two physical parameters are separated, they can be directly used to detect anomalies and predict the variation in material properties such as electrical conductivity, magnetic permeability and microstructure. This paper reports physical interpretation of these two physical phenomena that can be found in different time responses given the ECPT image sequences. Based on the phenomenon and their behaviors, the paper proposes a statistical method based on single channel blind source separation to decompose the two physical phenomena using different stages of eddy current and thermal propagation from the ECPT images. Links between mathematical models and physical models have been discussed and verified. This fundamental understanding of transient eddy current distribution and heating propagation can be applied to the development of feature extraction and pattern recognition for the quantitative analysis of ECPT measurement images and defect characterization. © *2013 American Institute of Physics*. [http://dx.doi.org/10.1063/1.4790866]

I. INTRODUCTION

Recently, the use of non-destructive testing (NDT) techniques have been increasingly developed and applied for inspection and monitoring of defects in both industrial and research fields. Electromagnetic, especially micro-magnetic, techniques have a special advantage for the application in NDT where electromagnetic and other properties are influenced by the same microstructure parameters and their changes. Furthermore, they are sensitive to load-induced and residual stresses. All electromagnetic and micro-magnetic techniques presented and applied in the NDT field are based on the cyclic magnetization (pulsed or sinusoidal) of a certain material volume.[1] These techniques can be categorized into methods based on either reversible or irreversible magnetization process realization. Electromagnetic NDT techniques are used to detect flaws, bond or weld integrity, thickness, electrical conductivity, and the presence of rebar or metals. As a result, a great number of electromagnetic NDT techniques have been developed such as eddy current (EC), magnetic flux leakage (MFL), magnetic Barkhausen noise (MBN), magneto acoustic emission (MAE), stress-induced magnetic anisotropy (SMA), metal magnetic memory (MMM),[2,3] etc.

Out of the above electromagnetic NDT techniques, the eddy current method is the most widely applied. Since the probe does not have to contact the work surface, eddy current testing is useful for rough surfaces and surfaces with wet films or coatings. Most analysis and design studies of eddy-current probes for non-destructive evaluation are based on the behavior of axially symmetric air-cored coils. Dodd and Deeds provided closed-form analytical expressions which are used to calculate their electromagnetic fields and impedances in the presence of multilayered conducting slabs or infinite cylindrical workpieces.[4] Bertotti showed the physical mechanism of eddy current losses in ferromagnetic materials.[5] Bowler *et al.* developed a general three-dimensional computational model of ferrite-core eddy current probes incorporating volume integral and conjugate gradient methods for research and design studies in non-destructive evaluation.[6] They also provided eddy-current probe impedance[7] and the inverse eddy current problem as the task of reconstructing an unknown distribution of electrical conductivity from eddy current probe impedance measurements recorded as a function of probe position and excitation frequency.[8] Park *et al.* interpreted the domain wall motion in the ion irradiated amorphous ribbon.[9]

In the above eddy current NDT, conventional techniques use a single frequency sinusoid as the input signal to excite structures under inspection. Pulsed eddy current (PEC) NDT is a recently developed method which uses a pulse excitation for structural inspection instead of a single frequency sinusoidal. This pulsed excitation simultaneously generates numerous frequencies on the sample during the testing. According to the inspection frequency and skin-depth relationship, PEC can penetrate different depths versus different

[a)]A. Yin and B. Gao contributed equally to this work.
[b)]Author to whom correspondence should be addressed. Electronic mail: bin.gao@ncl.ac.uk.

frequencies comparing to EC with single frequency sinusoidal and providing several useful parameters such as defect size and location. PEC has been employed in several applications such as metal thickness measurement,[10] defect detection in multi-layered structures,[11] stress measurement,[12] defect and wall thinning detection in stainless steel pipes,[13] and corrosion detection[14] amongst others. PEC based characterization theories and feature extraction techniques have also been developed. Tian *et al*. investigated wavelet-based principal component analysis (PCA) defect classification and quantification for PEC NDT.[15] The authors also focused on transient analysis in the time-domain,[16] independent component analysis (ICA),[17] and shape features.[18] Morabito also proposed ICA for feature extraction.[19] Tsuboi *et al*. used the Fourier transform method and time-stepping method for numerical analysis of PEC testing.[20] For evaluating complex geometry components defects and material characterization such as turbine blades and gears, Tian *et al*. developed magnetic sensor arrays for PEC systems.[21] Mandache and Lefebvre applied different techniques to reduce the lift-off effects.[22] However, magnetic sensor arrays for non-destructive testing and evaluation (NDT&E) have limitations such as low spatial resolution, low sensitivity, and inferred by stand-off measurement distance.[21,23]

The above problems can be solved by integrating eddy current and thermography techniques leading to the eddy current pulsed thermography (ECPT) (or pulsed eddy current thermography).[24,25] During this testing, a high-current electromagnetic pulse is employed to induce eddy current in the conductive material under inspection for a short period (typically less than 1 s). This will result in surface heat distribution from Joule heating and heat diffusion procedure. An infrared camera is used to detect anomalies. Wilson *et al*. applied numerical modeling with COMSOL and experimental studies to understand the EC stimulated thermography.[25] The major advantage of thermography over other techniques is the potential of accurate non-contact inspection of a large area within a short period and large stand-off distances.[26] This technique has been applied for conductive composite defect inspection and classification,[27] crack detection of rolling contact fatigue of rail tracks,[28] glass fiber reinforced polymer specimen,[29] and power electronic devices.[30] The information richness of ECPT transient pattern has attracted a wide range of interests. He *et al*. compared two detections modes (transmission mode and reflection mode) for wall thinning and inner defect characterization using time to peak.[31] Bai employed ECPT for steel stress characterization using peak value.[32] Liang and Gui Yun *et al*. evaluated notches in carbon fiber reinforced plastic material through analysis of the surface heating pattern.[27] To enhance the flaw contrast and improve noise rejection qualities, pattern based image enhancement has been conducted. Maldague and Marinetti applied the Fourier transform to pulsed thermography, and enhanced the flaw-contrast significantly using a phase map.[33] Chatterjee and Tuli removed influence of non-uniform heating and surface emissivity variation using a Fourier transformation based image reconstruction algorithm.[34] Marinetti *et al*. employed PCA and ICA to improve the extraction of thermography features in water leakage identification and improve the flaw directivity with thermography.[35,36]

All of the above cited research recognizes that the basic physical mechanism corresponding to the general behavior of ECPT is the result of Joule heating via eddy current and heat diffusion. However, the research rarely discusses the key physical issues, such as what different effects do these two physical phenomena have in heating and cooling procedures, and reasons as to why the above algorithms can enhance the spatial and time resolution, and how the procedure links to the physical model are not clear. In this paper, physical interpretation of eddy current pulsed thermography is reported. Transient thermal responses and their temporal behaviors are found and verified through thermal distribution patterns of eddy current and thermal propagation. A statistical method based on single channel blind source separation (SCBSS) is developed to extract transient thermal patterns which are used to decompose the two physical phenomena given the different stages of eddy current and thermal propagation. Both mathematical and physical models are discussed. Experimental studies have been conducted to show the efficiency of pattern extraction and physical interpretation.

The paper is organized as follows: Sec. II discusses the linkage between mathematical model and physical model of ECPT; Sec. III introduces the experimental set-up; Sec. IV presents the experiment results. The conclusions are given in Sec. V.

II. THEORY AND METHOD

A. Pulsed eddy current and heat conduction

PEC response (EC) can be represented as a function of the system with the detected sample using Eq. (1)

$$P = f(\sigma, \mu, l, \xi, \theta), \tag{1}$$

where ξ denotes the sensor geometry factor, θ denotes the parameters of the excitation (frequency, amplitude, etc.), σ denotes the electrical conductivity of material, μ denotes the magnetic permeability of the material, and l denotes the lift-off (distance between the sensor and sample).

For a homogeneous field excitation parallel to the surface, the penetration depth of a magnetic field in a material is governed by the skin effect. The skin depth or penetration depth δ is given by

$$\delta = \frac{1}{\sqrt{f\pi\mu\sigma}}, \tag{2}$$

where f is the frequency of the pulsed excitation. This penetration depth δ decrease with increased frequency of the pulsed excitation f. EC density is mainly focused on surface-near zones of the material.

In previous work, the analysis is predominantly focused on the time response signal. Fig. 1 shows typical PEC responses in half period where the time is normalised to the repetition period of the excitation. As shown in Fig. 1(a), B_{REF} is the reference signal obtained from a defect-free material or air[11] and B is the time response of the detected area.

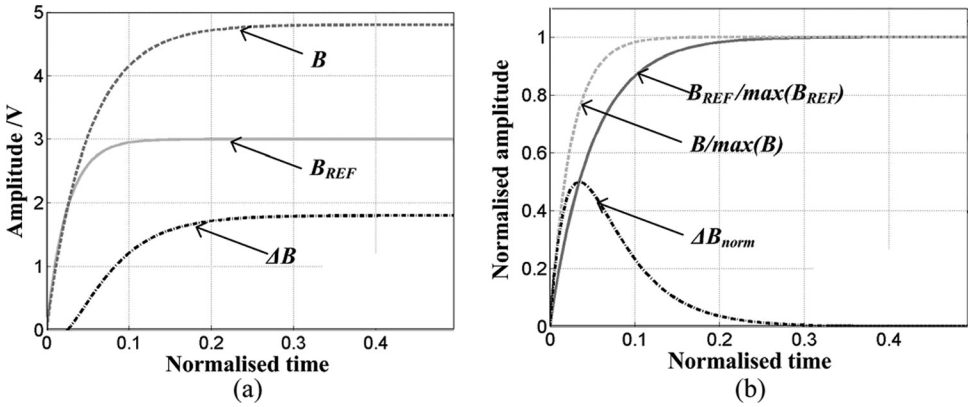

FIG. 1. (a) PEC time domain transient responses in half period and (b) normalised amplitude responses.

It is convenient to quantify the differential signal (ΔB) or balance signal[37] as shown in Eq. (3)

$$\Delta B = B - B_{REF}. \tag{3}$$

For Fig. 1 and Eq. (1), the influence of conductivity σ is prominent in the rising edge such that the magnetic flux density decreases as the conductivity variation increases. Here, σ is inversely proportional to electrical intensity which explains the inverse relation between conductivity and magnetic induction B. The ΔB_{norm} consistently decrease as the increased conductivity. The influence of permeability μ is prominent in the stable phase of the transient response. As permeability increases, the values of non-normalized B also increases and shows no significant change in the rising edge of the PEC response.[37] The lift-off has a strong influence on the acquired signals for either the voltage or magnetic field signal measurements. Harmonic lift-off invariance points occur due to amplitude and phase shift variation with lift-off.[22] The sensor geometry factor ξ also influences the distribution and density of the EC.[4–6]

When an EM field is applied to a conductive material, the temperature increases owing to resistive heating from the induced electric current. This is known as Joule heating. The sum of the generated resistive heat Q is proportional to the square of the magnitude of the electric current density J_s. Current density, in turn, is proportional to the electric field intensity vector E. The following equation expresses this relationship:

$$Q = \frac{1}{\sigma}|J_s|^2 = \frac{1}{\sigma}|\sigma E|^2, \tag{4}$$

where electric conductivity σ is dependent on temperature and is given by

$$\sigma = \frac{\sigma_0}{1 + \alpha(T - T_0)},$$

where σ_0 is the conductivity at the reference temperature T_0 and α is the temperature coefficient of resistivity, which describes how resistivity varies with temperature.[25] Note that σ is inversely proportional to temperature T.

In general, by taking account of heat diffusion and Joule heating, the heat conduction equation of a specimen can be expressed as

$$\frac{\partial T}{\partial t} = \frac{\lambda}{\rho C_p}\left(\frac{\partial^2 T}{\partial x^2} + \frac{\partial^2 T}{\partial y^2} + \frac{\partial^2 T}{\partial z^2}\right) + \frac{1}{\rho C_p} q(x, y, z, t), \tag{5}$$

where $T = T(x, y, z, t)$ is the temperature distribution, λ is the thermal conductivity of the material (W/m K), which is dependant on temperature. ρ is the density (kg/m^3), C_p is specific heat (J/kg K). $q(x, y, z, t)$ is the internal heat generation function per unit volume, which is the result of the eddy current excitation.[25]

The variation of temporal temperature depends on the spatial temperature variation for heat conduction. Fourier's law of heat conduction states that the time rate of heat transfer through a material is proportional to the negative gradient in the temperature and to the cross section area of the material. Thus, the heat diffusion rate increases along with the increased temperature as difference between $T(x, y, z, t)$ in (x, y, z) and all other locations round about it (environment). In general, the thermal conductivity λ decreases as $T(x, y, z, t)$ variation increases for pure metal material and the eddy current generates Joule heating as denoted as $q(x, y, z, t)$ According to Eqs. (1) and (4), it is influenced by $T(x, y, z, t)$, ξ, θ, σ, μ, and l, which have been demonstrated as mentioned before. At the same time, because $q(x, y, z, t)$ increases quickly from initial stable state (zero) to stable state of EC, it is too fast to significantly effect the heat diffusion in this transient phase. Hence, the $q(x, y, z, t)$ will maintain steady stable state and the effects of heat diffusion takes an important role in this stage. At last, the two physical procedures reach equilibrium state. In other words, the two thermal phenomenons play a different role in different phase of the heat conduction in Eq. (5), which will be further detailed in Sec. IV A.

The resultant surface heat distribution from Joule heating and the heat diffusion procedure is recorded using a thermographic sensor, e.g., an infrared camera. Thus, the recorded video shows the variation of temporal temperature. Fig. 2 shows the mathematical representation of the image frames from a recorded video.

B. Patterns extraction of ECPT using single channel blind source separation

In line with Eq. (5), the derivative of the thermography image sequences captured by the infrared camera can be considered as an observation $\mathbf{Y}(t)$, which is mixed with the Joule

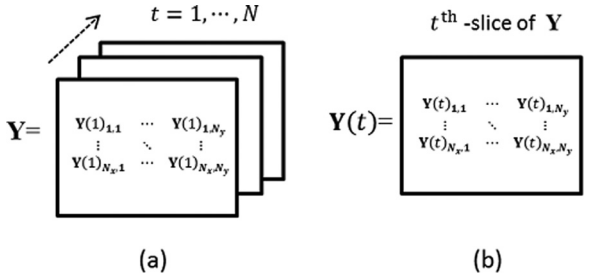

FIG. 2. (a) Tensor representation of the image sequences **Y** and (b) the *t*th frame of **Y**.

heating of eddy current and the heat diffusion. In other words, the observation is assumed to be a mixture of two sources and additive noise with their mixing weight, $m_i, (i = 1, 2, 3)$. The mathematical definition of the mixing model can be described as

$$\underbrace{\frac{\partial T}{\partial t}}_{\mathbf{Y}(t)} = \underbrace{\frac{\lambda}{\rho C_p}\left(\frac{\partial^2 T}{\partial x^2} + \frac{\partial^2 T}{\partial y^2} + \frac{\partial^2 T}{\partial z^2}\right)}_{m_1\mathbf{X}_1(t)} + \underbrace{q(x,y,z,t)}_{m_2\mathbf{X}_2(t)} + \underbrace{n(x,y,z,t)}_{m_3\mathbf{X}_3(t)}, \tag{6}$$

where $N_s = 3$ denotes the number of sources. $\mathbf{X}_1(t)$ refers to the source represented by Joule heating of eddy current, $\mathbf{X}_2(t)$ refers to the source represented by heat diffusion, and $\mathbf{X}_3(t)$ refers to the noise which represents other factors such as various thermal radiation surroundings. In this study, dimensions $N_x \times N_y$ are defined by the infrared camera sensor array with setting as $N_x = 64$, $N_y = 80$. Equation (6) is the special case of underdetermined blind source separation problem where $N_o = 1$ ($N_o \ll N_s$, N_o denotes the number of sensor), termed as SCBSS.[38]

To solve the above ill-posed problem ($N_o \ll N_s$), we adopt a decomposition-based approach as the generative model. This approach was employed formerly in analyzing non-stationary sources by expressing a fixed-length segment drawn from transient response, such that continuous transient slices of length N can be chopped out of a set of image sequences from t to $t + N - 1$, and the subsequent segment is denoted as equivalent as derivative image sequences captured by N independent infrared cameras $\mathbf{Y}'(t) = [\mathrm{vec}(\mathbf{Y}(t)), \mathrm{vec}(\mathbf{Y}(t+1)), \ldots, \mathrm{vec}(\mathbf{Y}(t+N-1))]^{\mathbf{T}}$, where "**T**" denotes transposed operator and "vec" denotes the vectorization operator. The constructed image sequences is then expressed as a linear combination of the signals generated by the sources such that $\mathbf{Y}'(t) = \mathbf{M}X'(t)$, where mixing matrix $\mathbf{M} = [\mathbf{m}_1, \ldots, \mathbf{m}_{N_s}]$ and $\mathbf{m}_i$ is the *i*th mixing vector and $\mathbf{X}'(t) = [\mathrm{vec}(\mathbf{X}_1(t)), \mathrm{vec}(\mathbf{X}_2(t)), \ldots, \mathrm{vec}(\mathbf{X}_{N_s}(t))]^{\mathbf{T}}$. Assuming that $N_s = N$ and **M** has full rank so that the transforms between $\mathbf{Y}'(t)$ and $\mathbf{X}'(t)$ be reversible in both directions such that the inverse matrix $\mathbf{W} = \mathbf{M}^{-1}$ exists. The purpose of this decomposition is to model the multivariate distribution of $\mathbf{Y}'(t)$ in a statistically efficient manner.

For convenience, the $\mathbf{Y}'(t)$ can be transformed into uncorrelated sources by means of a whitening matrix use the eigenvalue decomposition (EVD)[39] of the covariance matrix $E\{\mathbf{Y}'(t)\mathbf{Y}'(t)^{\mathbf{T}}\} = \mathbf{EDE}^{\mathbf{T}}$, where **E** is the orthogonal matrix of eigenvectors and $\mathbf{D} = \mathrm{diag}(\lambda_1, \ldots, \lambda_N)$, being $\lambda_1 \geq \ldots \geq \lambda_N$ the eigenvalues. We can rewrite $E\{\mathbf{Y}'(t)\mathbf{Y}'(t)^{\mathbf{T}}\}$ as

$$\begin{aligned} E\{\mathbf{Y}'(t)\mathbf{Y}'(t)^{\mathbf{T}}\} &= \mathbf{EDE}^{\mathbf{T}} = \mathbf{ED}^{1/2}\mathbf{D}^{1/2}\mathbf{E}^{\mathbf{T}} \\ &= E\{\mathbf{W}_{PCA}^{-1}\mathbf{X}'_{PCA}(t)\mathbf{X}'_{PCA}(t)^{\mathbf{T}}\mathbf{W}_{PCA}^{-\mathbf{T}}\} \\ &= \mathbf{W}_{PCA}^{-1}E\{\mathbf{X}'_{PCA}(t)\mathbf{X}'_{PCA}(t)^{\mathbf{T}}\}\mathbf{W}_{PCA}^{-\mathbf{T}} \\ &= \mathbf{W}_{PCA}^{-1}\mathbf{W}_{PCA.}^{-\mathbf{T}}. \end{aligned} \tag{7}$$

In Eq. (7), $E\{\mathbf{X}'_{PCA}(t)\mathbf{X}'_{PCA}(t)^{\mathbf{T}}\} = \mathbf{I}$ where **I** is identity matrix. Thus, $\mathbf{W}_{PCA} = (\mathbf{ED}^{1/2})^{-1} = \mathbf{D}^{-1/2}\mathbf{E}^{\mathbf{T}}$ and whitening can now be done, namely

$$\mathbf{X}'_{PCA}(t) = \widehat{\mathbf{W}}_{PCA}\mathbf{Y}'(t), \tag{8}$$

where $\widehat{\mathbf{W}}_{PCA}$ is the estimated inverse matrix and $\mathbf{X}'_{PCA}(t)$ is the estimated sources by using the PCA. After using PCA to obtain the uncorrelated sources, it is also possible to reduce the transformed output dimension, e.g., choosing $N_s \leq N$, there exits N_s. In this paper, we set $N_s = 1$ which denotes the number of separated sources. In the mathematical approach, the first separated source, i.e., the eigenvector with the largest value of λ_1, is the direction along which the data have the most variance and it already accounts for above 90% of the whole Eigen values. According to the physical model as discussed in Sec. II A, Joule heating and heat diffusion are two key physical parameters influencing heat flow during the transient response period. During the short moment of the EC excitation, the influence of Joule heating is maximal, whereas the influence of heat diffusion is minimal. Then after, the influence of Joule heating is minimal, whereas the influence of heat diffusion is maximal. And finally reaching a new balance, both physical parameters influence the heat flow. Thus, with respected mathematic model, it is reasonable assuming that the first separated source (1st PC) directly refers the phenomenon whether heat diffusion or Joule heating takes the dominant role in different stages.

III. EXPERIMENT SETUP

The experiment setup is shown in Fig. 3. An Easyheat 224 from Cheltenham Induction Heating is used for coil excitation. The Easyheat has a maximum excitation power of 2.4 kW, a maximum current of 400 Arms, and an excitation

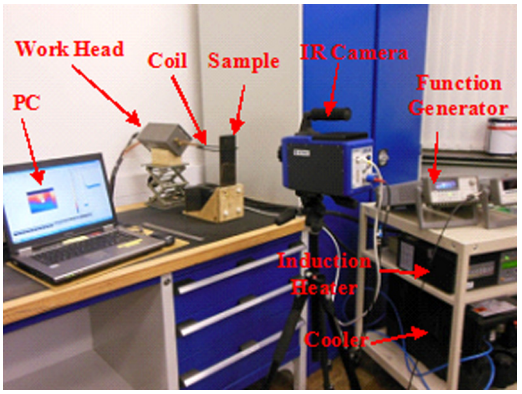

FIG. 3. Experiment setup.

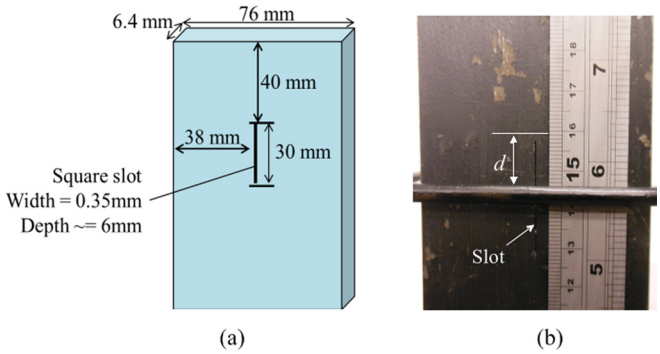

FIG. 4. (a) Steel sample with slot and (b) sample with inductor (coil).

frequency range of 150–400 kHz (200 Arms and 256 kHz are used during this study). This measurement system has a quoted rise time (the heating period to full power) of 5 ms, which was verified experimentally. Water cooling of coil is implemented to counteract direct heating of the coil.[24]

An SC7500 IR camera is a Stirling cooled camera with a 320 × 256 array of 1.5–5 μm InSb detectors. This camera has a sensitivity of <20 mK and a maximum full frame rate of 383 Hz, with the option to increase frame rate with windowing of the image. A rectangular coil is constructed to apply directional excitation. This coil is made of 6.35 mm high conductivity hollow copper tube. During the experiment, only one edge of the rectangular coil is used to stimulate eddy current to the underneath sample. In this study, the frame rate is 2000 Hz with a 320 × 256 array, and 2 s videos are recorded in the experiments.

The mild steel sample shown in Fig. 4(a), containing a narrow, surface breaking slot has been introduced in Ref. 25. A 400 ms heating duration is selected for inspection, which is long enough to elicit an observable heat pattern.

IV. RESULTS AND DISCUSSION

A. Temperature distribution and transient responses of ECPT

Wilson *et al.* studied transient EC distribution and heating propagation at steel samples with slots.[25] They illustrated that the eddy current distribution around the slot was changed for various d as shown in Fig. 4(b). When the depth of defect is not deep (shorter d), the situation where ECs cannot flow underneath the defect, hence are forced to flow around the end of the defect, leading to regions of high EC density and resulting in hot areas at the tips of the defect and regions at either side of the defect where ECs are forced to spread out with, resulting in cooler areas. When the depth of defect is deep (longer d), the situation where ECs are forced to flow under the defect, leading to a higher EC density and resultant heating at the bottom of the defect.

Fig. 5 shows the temperature distribution at the sample surface from the experiment for d = 4 mm. When the inductor is close to the tip of the defect (d = 4 mm), there is significant EC flow around the tip of the defect and the defect behaves predominantly as a slot. Because the emissivity of the sample is unknown, digital level (dl) is used to describe the temperature rather than °C. According to Eq. (6), 1st

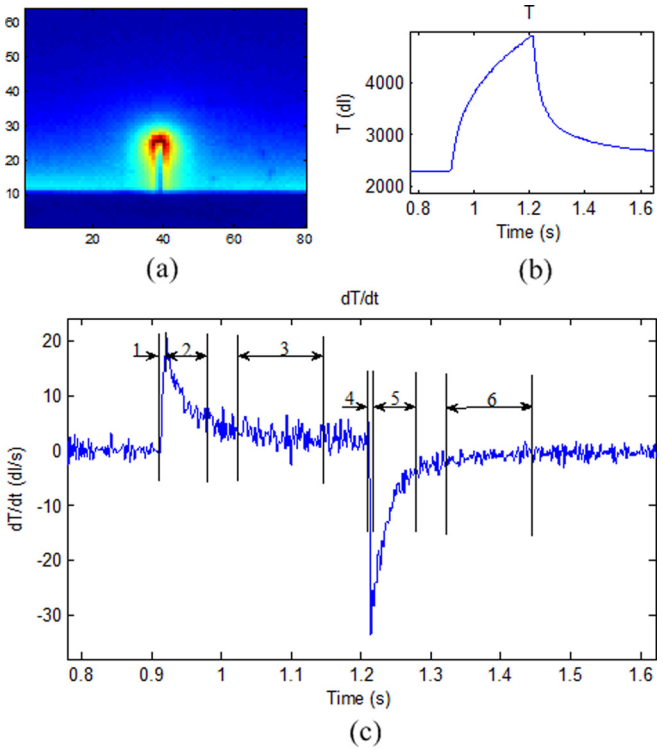

FIG. 5. (a) Thermal image with $d = 4$ mm at 0.1 s after heating, (b) transient temperature response at impact point against time, and (c) 1st derivatives of temperature response.

derivatives of temperature response is composed of heat diffusion and Joule heating. From Figs. 5(c) and 1, the thermal video based heat conduction procedure can be obviously divided into 6 phases as shown in Fig. 5(c).

- Phase 1: A resultant singular electric current field is generated and eddy current quickly rises from zero to maximum, then retains steady state.[13] This phase is very short (about 5 ms), whereas heat diffusion does not play an obvious role as can be considered zero or a small value. For Eq. (6), we only take into account Joule heating in this phase.
- Phase 2: Electric current field maintains a stable state. The sum of the generated resistive heat Q is constant. However, heat diffusion velocity gradually increases following a different temperature increase according to Fourier's law of heat conduction. Simultaneously, heat diffusion is getting more obvious because of the significant heating propagation time. Heat diffusion plays a main role for thermal video in this phase.
- Phase 3: Heat conduction also reaches equilibrium state. The sum of the generated resistive heat Q and heat diffusion are at equilibrium in this phase.
- Phase 4: Eddy current quickly decreases from maximum to zero when exciting signal is stopped. Similar to the first phase, the procedure is very short, which lasts about 5 ms. Changing of heat diffusion is not sharp in such a short time. Joule heating plays a main role for thermal video in this phase.
- Phase 5: There is no eddy current in this phase, so $q(x,y,z,t)$ can be omitted in Eq. (6). The changing of 1st

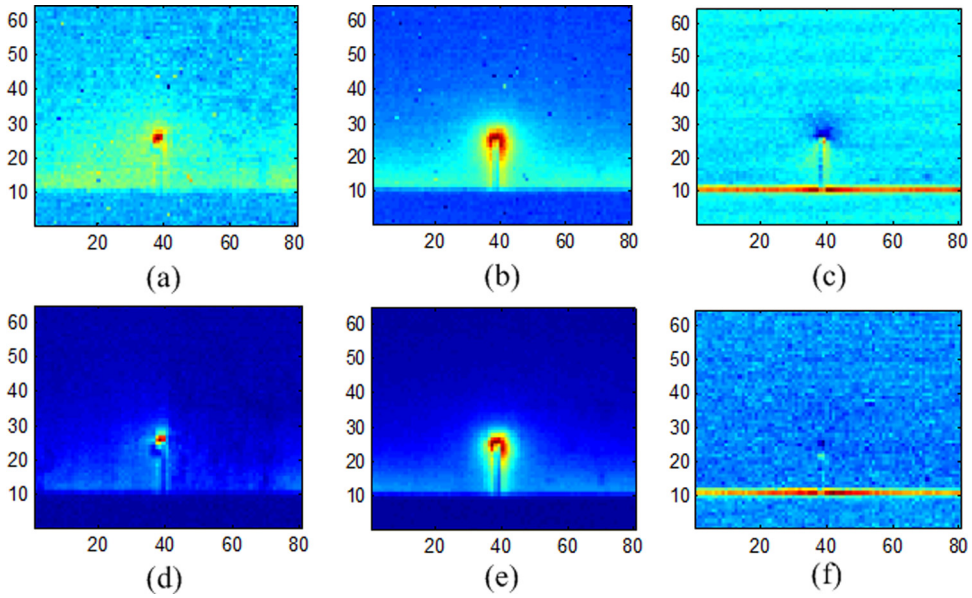

FIG. 6. Principal component extraction of different phase with $d = 4$ mm: (a) first phase; (b) second phase; (c) third phase; (d) forth phase; (e) fifth phase; (f) sixth phase.

derivatives is resulted from the velocity variation of heat diffusion.

- Phase 6: Heat diffusion is at a stable state.

B. Transient patterns of different phases

To verify the transient behaviours of temperature, pattern extraction using PCA based SCBSS method is applied. The specific steps are as follows: (1) The first derivative of temperature against time dT/dt-t at the impact point is calculated for partition purpose as mentioned in Sec. IV A. The partition results are shown in Fig. 5(c). (2) Given the 6 partitioned phases as shown in Fig. 5(c), the ECPT video is divided into 6 parts against time. (3) According to Eq. (6), the first derivative of whole thermal video against time is calculated. (4) Principal components of each part are extracted using PCA based SCBSS method. The results are shown in Fig. 6.

In Fig. 6, only first principal component for each phase is shown. In Fig. 6, the two physical phenomenon of eddy current and thermal propagation are clearly extracted. In the first phase, Joule heating plays an important role. According to Ref. 25, ECs are forced to flow around the end of the slot, leading to regions of most high EC density and resulting in hot areas at tips of the slot, which is shown in Fig. 6(a). At the same time, the regions close to the coil have equivalent EC density which results hot areas. Hence, the principal component indicates the heating of EC. In Fig. 6(b), the principal component mainly means heat diffusion. Joule heating $q(x,y,z,t)$ maintains stable state, and heat diffusion is varying in this phase. The velocity of heat diffusion is lower at the region around the end of the slot than other areas, and this results hot areas locating at both tips and sides of the slot. In Fig. 6(c), the sum of $q(x,y,z,t)$ and heat diffusion is at equilibrium. The principal component reflects the various thermal radiation surroundings. Heating procedure of the forth phase is as same as the first phase. The principal component mainly indicates the heating of EC. However, compare to Fig. 6(a), hot area is more concentrated in Fig. 6(d). The reason is that surface temperature is higher in this phase and the temperature difference is smaller, which leads to lower heat conduction velocity. Similar to Fig. 6(b), heat diffusion is the main factor in Fig. 6(e). However, it is at lower heat conduction velocity than that of Fig. 6(b). Finally, there only exists heat diffusion in Fig. 6(f), and it is maintained at stable state. The principal component reflects the various thermal radiation surroundings.

Fig. 7 shows principal components of the first derivative for whole thermal video. Fig. 7(b) indicates influences of radiation surroundings. As can be seen from Fig. 7(a), it is difficult to distinguish whether the displayed phenomenon is from transient PEC distribution or from heating propagation. In fact, the PCA based SCBSS process of whole video mainly takes into account the heating propagation and therefore only these parts are reflected in Fig. 7.

Fig. 8 shows principal components of different phase for test sample ($d = 14$ mm). The principal component mainly indicates the eddy current heating procedure in Figs. 8(a) and 8(d). According to Ref. 25, ECs are forced to flow under the slot, so hot areas are obviously not at the tips of the slot and regions at both sides of the slot. However, for Figs. 8(b) and 8(e), heat diffusion plays a decisive role. At the same time, the velocity of heat diffusion is lower at the region around the end of the slot than other areas, and this results in hot areas locating at both tips and sides of the slot. Thus, it is

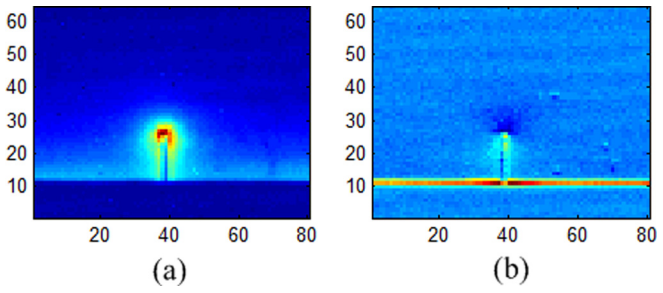

FIG. 7. Principal components of whole thermal image with $d = 4$ mm: (a) the first principal component; (b) the second principal component.

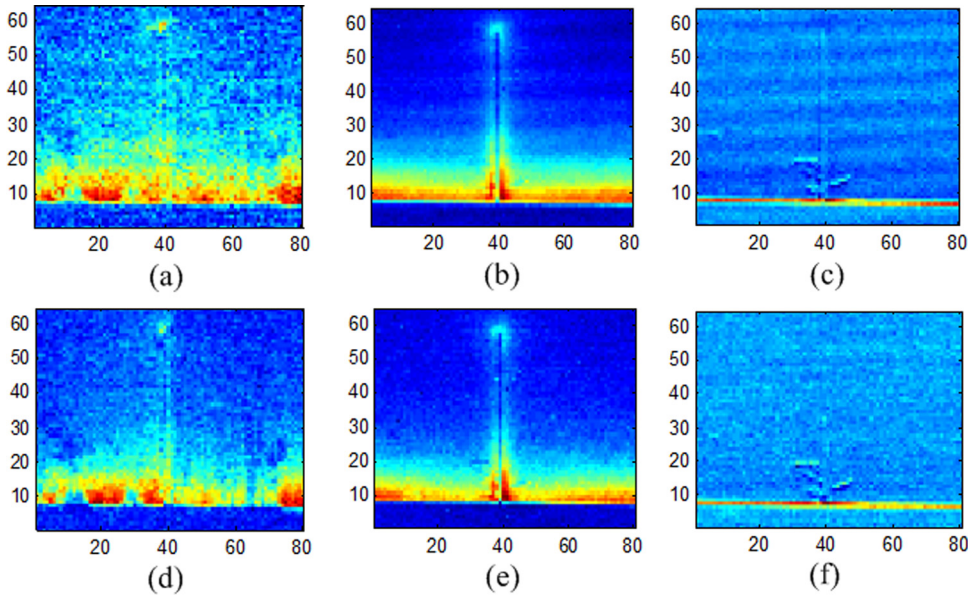

FIG. 8. Principal component extraction of different phase with $d = 14$ mm: (a) first phase; (b) second phase; (c) third phase; (d) forth phase; (e) fifth phase; (f) sixth phase.

clear to visualize the shape of slot in Figs 8(b) and 8(e). For Figs. 8(c) and 8(f), the principal component reflects the various thermal radiation surroundings.

Fig. 9 shows the principal components of the first derivative for whole thermal video. Similar to Fig. 7, the principal components mainly indicate heating propagation. Fig. 9 cannot clearly identify the two physical phenomenon of eddy current and thermal propagation. These separated patterns can be verified by previous simulation studies.[25]

V. CONCLUSIONS AND FUTURE WORK

In this paper, two physical effects in eddy current pulsed thermography are found and the physical interpretation is reported. Based on the differentiation, a single channel blind source separation method is proposed for transient pattern extraction of ECPT video. The linkage between mathematical and physical explanations has been presented. The conclusions can be drawn as follows:

(1) The basic physical mechanism responsible for the general behavior of ECPT is recognized in an accumulation of Joule heating and heat diffusion. Physical interpretation of eddy current pulsed thermography is reported to decouple the two physical phenomenon of eddy current and thermal propagation in different phases of ECPT. The two physical effects have different temporal behaviors. This fundamental understanding of transient PEC distribution and heating propagation will aid in the quantitative analysis of ECPT images and defect characterization.

(2) The patterns of transient heat distribution in different phases of ECPT are extracted by using a PCA based SCBSS algorithm. The linkage between mathematical and physical models is discussed. Transient heat distribution in short time is compared to that of whole ECPT video. The physical interpretations are verified by transient patterns.

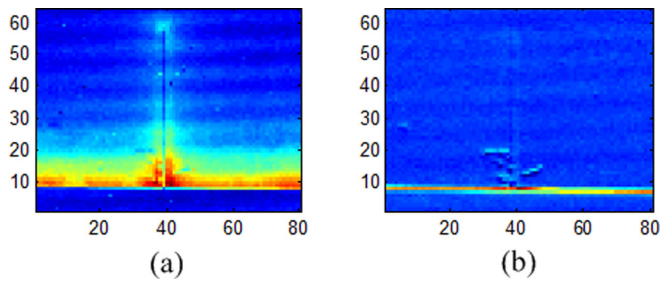

FIG. 9. Principal components of whole thermal image with $d = 14$ mm: (a) the first principal component; (b) the second principal component.

Future work would be focused on the method and how to apply different physical transient phases and their behaviors on comprehensive defect detection and characterization. Pattern separation of Joule heating from eddy current, heat diffusion, and other impacts needs further research to accurately extract independent components from observed transient responses. The knowledge gained from these tests is applied to EC thermography to real defects in ex-service components, such as quantitative analysis of ECPT images and defect characterization through multiple physics for interpretation.

ACKNOWLEDGMENTS

This project was funded by EPSRC (EP/E005071/1) and the National Natural Science Foundation of China (Grant No. 51105396). This work was also funded by Chongqing University of China and Newcastle University. Aijun Yin would like to thank Chinese Scholar Council (CSC) to fund him to undertake one year visiting study at Newcastle University.

[1]I. Altpeter, R. Becker, G. Dobmann, R. Kern, W. Theiner, and A. Yashan, "Robust solutions of inverse problems in electromagnetic non-destructive evaluation," Inverse Probl. **18**(6), 1907–1921 (2002).
[2]K. Miya, "Recent advancement of electromagnetic nondestructive inspection technology in Japan," IEEE Trans. Magn. **38**(2), 321–326 (2002).
[3]Z. D. Wang, Y. Gu, and Y. S. Wang, "A review of three magnetic NDT technologies," J. Magn. Magn. Mater. **324**(4), 382–388 (2012).
[4]C. V. Dodd and W. E. Deeds, "Analytical solutions to eddy-current probe-coil problems," J. Appl. Phys. **39**(6), 2829–2838 (1968).

[5]G. Bertotti, "Physical interpretation of eddy current losses in ferromagnetic materials. I. Theoretical considerations," J. Appl. Phys. **57**(6), 2110–2117 (1985).
[6]J. R. Bowler, L. D. Sabbagh, and H. A. Sabbagh, "Theoretical and computational model of eddy-current probes incorporating volume integral and conjugate gradient methods," IEEE Trans. Magn. **25**(3), 2650–2664 (1989).
[7]J. R. Bowler, S. A. Jenkins, L. D. Sabbagh, and H. A. Sabbagh, "Eddy-current probe impedance due to a volumetric flaw," J. Appl. Phys. **70**(3), 1107–1114 (1991).
[8]S. J. Norton and J. R. Bowler, "Theory of eddy current inversion," J. Appl. Phys. **73**(2), 501–512 (1993).
[9]D. G. Park, H. Song, C. Y. Park, C. S. Angani, C. G. Kim, and Y. M. Cheong, "Analysis of the domain wall motion in the ion irradiated amorphous ribbon," IEEE Trans. Magn. **45**(10), 4475–4477 (2009).
[10]H. C. Yang and C. C. Tai, "Pulsed eddy-current measurement of a conducting coating on a magnetic metal plate," Meas. Sci. Technol. **13**(8), 1259–1265 (2002).
[11]R. A. Smith and G. R. Hugo, "Transient eddy current NDE for ageing aircraft—capabilities and limitations," Insight: Non-Destr. Test. Cond. Monit. **43**(1), 14–25 (2001).
[12]M. Morozov, G. Yun Tian, and P. J. Withers, "The pulsed eddy current response to applied loading of various aluminium alloys," NDT & E Int. **43**(6), 493–500 (2010).
[13]C. S. Angani, D. G. Park, C. G. Kim, P. Leela, and M. Kishore, "Pulsed eddy current differential probe to detect the defects in a stainless steel pipe," J. Appl. Phys. **109**(7), 07D348 (2011).
[14]Y. He, G. Tian, H. Zhang, M. Alamin, A. Simm, and P. Jackson, "Steel corrosion characterization using pulsed eddy current systems," IEEE Sens. J. **12**(6), 2113–2120 (2012).
[15]G. Y. Tian, A. Sophian, D. Taylor, and J. Rudlin, "Wavelet-based PCA defect classification and quantification for pulsed eddy current NDT," IEE Proc.-A: Sci., Meas. Technol. **152**(4), 141–148 (2005).
[16]Y. He, F. Luo, M. Pan, X. Hu, B. Liu, and J. Gao, "Defect edge identification with rectangular pulsed eddy current sensor based on transient response signals," NDT & E Int. **43**(5), 409–415 (2010).
[17]G. Yang, G. Y. Tian, P. W. Que, and T. L. Chen, "Independent component analysis-based feature extraction technique for defect classification applied for pulsed eddy current NDE," Res. Nondestruct. Eval. **20**(4), 230–245 (2009).
[18]T. Chen, G. Y. Tian, A. Sophian, and P. W. Que, "Feature extraction and selection for defect classification of pulsed eddy current NDT," NDT & E Int. **41**(6), 467–476 (2008).
[19]C. F. Morabito, "Independent component analysis and feature extraction techniques for NDT data," Mater. Eval. **58**(1), 85–92 (2000).
[20]H. Tsuboi, N. Seshima, I. Sebestyén, J. Pavo, S. Gyimothy, and A. Gasparics, "Transient eddy current analysis of pulsed eddy current testing by finite element method," IEEE Trans. Magn. **40**(2), 1330–1333 (2004).
[21]G. Y. Tian, A. Sophian, D. Taylor, and J. Rudlin, "Multiple sensors on pulsed eddy-current detection for 3-D subsurface crack assessment," IEEE Sens. J. **5**(1), 90–96 (2005).
[22]C. Mandache and J. H. V. Lefebvre, "Transient and harmonic eddy currents: Lift-off point of intersection," NDT & E Int. **39**(1), 57–60 (2006).
[23]J. Hwang, J. Lee, and S. Kwon, "The application of a differential-type Hall sensors array to the nondestructive testing of express train wheels," NDT & E Int. **42**(1), 34–41 (2009).
[24]J. Wilson, G. Y. Tian, I. Z. Abidin, S. Yang, and D. Almond, "Pulsed eddy current thermography: System development and evaluation," Insight: Non-Destr. Test. Cond. Monit. **52**(2), 87–90 (2010).
[25]J. Wilson, G. Y. Tian, I. Z. Abidin, S. Yang, and D. Almond, "Modelling and evaluation of eddy current stimulated thermography," Nondestr. Test. Eval. **25**(3), 205–218 (2010).
[26]N. P. Avdelidis, B. C. Hawtin, and D. P. Almond, "Transient thermography in the assessment of defects of aircraft composites," NDT & E Int. **36**(6), 433–439 (2003).
[27]C. Liang and T. Gui Yun, "Surface crack detection for carbon fiber reinforced plastic (CFRP) materials using pulsed eddy current thermography," IEEE Sens. J. **11**(12), 3261–3268 (2011).
[28]J. Wilson, G. Tian, I. Mukriz, and D. Almond, "PEC thermography for imaging multiple cracks from rolling contact fatigue," NDT & E Int. **44**(6), 505–512 (2011).
[29]Z. Zeng, N. Tao, L. Feng, and C. Zhang, "Specified value based defect depth prediction using pulsed thermography," J. Appl. Phys. **112**(2), 023112 (2012).
[30]S. Huth, O. Breitenstein, A. Huber, and U. Lambert, "Localization of gate oxide integrity defects in silicon metal-oxide-semiconductor structures with lock-in IR thermography," J. Appl. Phys. **88**(7), 4000–4003 (2000).
[31]Y. He, M. Pan, and F. Luo, "Defect characterisation based on heat diffusion using induction thermography testing," Rev. Sci. Instrum. **83**(10), 104702 (2012).
[32]G. Y. T. L. B. Bai, "Stress measurement by pulsed thermography using eddy current heating," in Proceedings of the 51th Annual Conference of BINDT, Northamptonshire, UK, 2012.
[33]X. Maldague and S. Marinetti, "Pulse phase infrared thermography," J. Appl. Phys. **79**(5), 2694–2698 (1996).
[34]K. Chatterjee and S. Tuli, "Image enhancement in transient lock-in thermography through time series reconstruction and spatial slope correction," IEEE Trans. Instrum. Meas. **61**(4), 1079–1089 (2012).
[35]S. Marinetti, E. Grinzato, P. G. Bison, E. Bozzi, M. Chimenti, G. Pieri, and O. Salvetti, "Statistical analysis of IR thermographic sequences by PCA," Infrared Phys. Technol. **46**(1–2), 85–91 (2004).
[36]A. A. Khan, V. Vrabie, J. I. Mars, A. Girard, and G. D'Urso, "A source separation technique for processing of thermometric data from fiber-optic DTS measurements for water leakage identification in dikes," IEEE Sens. J. **8**(7), 1118–1129 (2008).
[37]I. Adewale and G. Tian, "Decoupling the influence of permeability and conductivity in pulsed eddy current measurements," IEEE Trans. Magn. **PP**(99), 1 (2012).
[38]G. Bin, W. L. Woo, and S. S. Dlay, "Single-channel source separation using EMD-subband variable regularized sparse features," IEEE Trans. Audio, Speech, Lang. Process. **19**(4), 961–976 (2011).
[39]A. Maćkiewicz and W. Ratajczak, "Principal components analysis (PCA)," Comput. Geosci. **19**(3), 303–342 (1993).